ORIGINAL ARTICLE

Journal
the American Ceramic Society

The effect of submicron grain size on thermal stability and mechanical properties of high-entropy carbide ceramics

Fei Wang[1]* | Xiang Zhang[1] | Xueliang Yan[1] | Yongfeng Lu[2] | Michael Nastasi[1,3,4] | Yan Chen[5] | Bai Cui[1,4]*

[1]Department of Mechanical & Materials Engineering, University of Nebraska–Lincoln, Lincoln, NE, USA

[2]Department of Electrical & Computer Engineering, University of Nebraska–Lincoln, Lincoln, NE, USA

[3]Nebraska Center for Energy Sciences Research, University of Nebraska–Lincoln, Lincoln, NE, USA

[4]Nebraska Center for Materials and Nanoscience, University of Nebraska–Lincoln, Lincoln, NE, USA

[5]Neutron Scattering Division, Oak Ridge National Laboratory, Oak Ridge, TN, USA

Correspondence
Bai Cui, Department of Mechanical & Materials Engineering, University of Nebraska–Lincoln, Lincoln, NE 68588, USA.
Email: bcui3@unl.edu

Abstract

$(Hf_{0.2}Zr_{0.2}Ta_{0.2}Nb_{0.2}Ti_{0.2})C$ high-entropy ceramics (HEC) with a submicron grain size of 400 to 600 nm were fabricated by spark plasma sintering using a two-step sintering process. Both X-ray and neutron diffractions confirmed the formation of single-phase with rock salt structure in the as-fabricated $(Hf_{0.2}Zr_{0.2}Ta_{0.2}Nb_{0.2}Ti_{0.2})C$ samples. The effect of submicron grain size on the thermal stability and mechanical properties of HEC was investigated. The grain growth kinetics in the fine-grained HEC was small at 1300 and 1600°C, suggesting high thermal stability that was possibly related to the compositional complexity and sluggish diffusion in HEC. Compared to the coarse-grain HEC with a grain size of 16.5 μm, the bending strength and fracture toughness of fine-grained HEC were 25% and 20% higher respectively. The improvement of mechanical properties in fine-grained HEC may be attributed to micromechanistic mechanisms such as crack deflection.

KEYWORDS

grain size, high-entropy ceramics, mechanical properties, spark plasma sintering, thermal stability

1 | INTRODUCTION

Compared to the extensively studied metallic high-entropy alloys (HEAs), high-entropy ceramics including oxide, borides, and carbides are less investigated. They are characterized by multiple metal elements in equal atomic concentrations in the cation position, while a nonmetal element

(such as O, B, or C) occupies the anion position. It is noted, however, that the chemical bonding in high-entropy carbide ceramics is primary covalent with secondary metallic bonding.[1,2] High-entropy ceramic materials have shown special physical properties. For example, the recent research on high-entropy carbides (HECs)[3-5] has revealed low thermal conductivity,[6] high hardness,[7-9] and an improved oxidation resistance.[10-12] These properties make HECs as promising candidate materials for high-temperature applications such

as the gas-cooled fast reactors and advanced combustion turbines. The promising properties of high-entropy ceramics have been attributed to the compositional complexity, significant lattice distortion, and sluggish diffusion.[1,6,13] However, the fundamental mechanisms about the relation between the high-entropy effects and the physical and chemical properties of ceramic materials remain poorly understood.

In ceramic materials, a decrease in grain size to sub-micrometers or nanometers can significantly improve the mechanical strength,[14] fracture toughness,[15,16] hardness,[17] radiation resistance, and induce superplasticity at high temperatures.[18,19] In spite of these benefits, the nanocrystalline grains become unstable and tend to grow at elevated temperatures, which is a significant limitation for high-temperature applications. The grain growth in ceramic materials is driven by the reduction in grain boundary energy[20] and accomplished by the grain-boundary migration.[21] Several strategies have been proposed to retard the grain growth of nanocrystalline ceramic materials, such as decreasing the grain-boundary migration rate by solute-drag or Zener pinning using dispersed fine particles[22] or reducing the grain-boundary energy by solute segregation.[23] However, these methods become less effective at temperatures above 1100°C.

We have explored a new concept to inhibit the grain growth in ceramic materials by the high-entropy effects. It was proposed that both the thermodynamic driving force (grain-boundary energy) and the kinetics (grain-boundary migration rate) of grain growth can be suppressed in HEC. The compositional complexity in HECs may decrease the grain-boundary energy by increasing grain-boundary complexity, while the sluggish diffusion in HECs may reduce the grain-boundary migration rates.

A two-step sintering method has been demonstrated as an effective way to sinter nanocrystalline ceramics with a high density and suppressed grain growth. During this process, the sample was first heated to a higher temperature to achieve an intermediate density and then quickly cooled down to a lower temperature and held a long time until it becomes fully dense. In the first higher temperature step, the sample can reach a critical density (70%–80%) at which the pores becomes unstable. In the second lower temperature step, full densification is achieved through diffusion (mass transport) along grain boundaries only while no grain-boundary migration occurs.[24] The two-step sintering process relies on the selection of an appropriate temperature at which the grain-boundary migration is suppressed while the grain-boundary diffusion is active. Chen et al[25] reported the fabrication of fully dense Y_2O_3 ceramics with a grain size of 60 nm by the two-step sintering method, which involves the initial heating at 1310°C and then sintering at 1150°C for 20 hours. Lee et al[26] also prepared nanocrystalline SiC ceramics with a grain size of 40 nm by initial heating at 1750°C and then at 1550°C for 8 hours.

The objective of this research is to investigate the effect of submicron grain size on the thermal stability and mechanical properties of HEC. Fine-grained $(Hf_{0.2}Zr_{0.2}Ta_{0.2}Nb_{0.2}Ti_{0.2})$C, with a submicrometer grain size, have been fabricated by spark plasma sintering (SPS) using the two-step sintering process. The grain growth kinetics have been examined by annealing at 1300 and 1600°C in an Ar atmosphere. The influence of grain size on the mechanical properties of HEC, such as hardness, bending strength, and fracture toughness, have been studied. The fundamental mechanisms about the microstructure-property relationship in fine-grained HECs have been revealed.

2 | EXPERIMENTAL PROCESS

Coarse powders of HfC (99.5%, <45 μm powder size), ZrC (99.5%, <45 μm), TaC (99.5%, <45 μm), NbC (99.0%, <45 μm), and TiC (99.5%, <45 μm) from Alfa Aesar were used for the synthesis of coarse-grained $(Hf_{0.2}Zr_{0.2}Ta_{0.2}Nb_{0.2}Ti_{0.2})$C sample. Fine powders of HfC (99.9%, 0.8 μm), ZrC (99.0%, 0.08 μm), TaC (99.0%, 1 μm), NbC (99.9%, 2 μm), and TiC (99.0%, 0.08 μm) from US Research Nanomaterials were used for the synthesis of fine-grained samples. HfC, TiC, TaC, NbC, and ZrC powders were mixed at an equimolar ratio with stainless steel grinding balls (ball-to-powder ratio: 5:1), followed by ball milling using a planetary ball mill (Model Pulverisette 7, Fritsch Gmbh) under Ar atmosphere. The coarse powders were ball milled with 10 mm diameter grinding balls at 250 rpm for 6 hours, while the fine powders were ball milled with 3 mm diameter grinding balls at 150 rpm for 2 hours. The ball milling process was paused for 5 minutes after every 15 minutes of milling to prevent overheating of the powders.

Spark plasma sintering (SPS) of the ball-milled powders was conducted on an SPS system (Model 10-4, Thermal Technologies) under vacuum (2×10^{-2} Torr). The SPS conditions for coarse-grained $(Hf_{0.2}Zr_{0.2}Ta_{0.2}Nb_{0.2}Ti_{0.2})$C were 2000°C for 5 minutes at a pressure of 30 MPa. The fine-grained $(Hf_{0.2}Zr_{0.2}Ta_{0.2}Nb_{0.2}Ti_{0.2})$C was synthesized by SPS using the two-step sintering process.[27] The temperature and time parameters are listed in Table 1. The pressure was kept at 30 MPa. The as-synthesized samples have a 20 mm diameter and 4 mm thickness.

The phase composition of $(Hf_{0.2}Zr_{0.2}Ta_{0.2}Nb_{0.2}Ti_{0.2})$C samples was analyzed by X-ray diffraction on a diffractometer (AXS D8 Discover, Bruker) operated at 40 kV and 44 mA with the Cu K_α radiation. Neutron diffraction experiment of the $(Hf_{0.2}Zr_{0.2}Ta_{0.2}Nb_{0.2}Ti_{0.2})$C sample was conducted using the VULCAN diffractometer at the Spallation Neutron Source in Oak Ridge National Laboratory.[28] Time-of-flight neutron diffraction patterns were collected in the high-resolution mode by two stationary detectors with

TABLE 1 The spark plasma sintering (SPS) conditions, measured density, relative density, grain size, and mechanical properties of $(Hf_{0.2}Zr_{0.2}Ta_{0.2}Nb_{0.2}Ti0_{0.2})C$ samples. C1 is the coarse-grained sample, while F-1 to F-3 are the fine-grained samples

Sample #	SPS conditions	Density (g/cm^3)/ relative density	Grain size (μm)	Hardness (GPa)	Bending strength (MPa)	Fracture toughness (MPam$^{1/2}$)
C-1	2000°C (5 min)	8.45/94.9%	16.5 ± 4.2	16.21 ± 1.04	318 ± 25	4.9 ± 0.5
F-1	2000°C (0.5 min) + 1800°C (15 min)	8.25/92.7%	0.578 ± 0.217	17.07 ± 0.54	400 ± 27	5.9 ± 0.7
F-2	1800°C (0.5 min) + 1600°C (15 min)	7.75/87.1%	0.421 ± 0.138	10.00 ± 1.12		
F-3	1600°C (3 min) + 1400°C (40 min)	7.64/85.8%	0.412 ± 0.149	9.79 ± 0.66		

$2\theta = \pm90°$, which measured the crystal planes (d-spacing in the range of 0.5-3.4Å) in parallel and perpendicular to the sample surface respectively. The neutron gauge volume was as large as $5 \times 10 \times 5$ mm^3 to provide sufficient statistics of the grains, and the volume center was aligned to the middle along the 4 mm thickness of the sample. Rietveld refinements of neutron diffraction data were performed using the General Structure Analysis System through the EXPGUI interface.[29,30]

Scanning electron microscopy (SEM) of microstructures was conducted on a FIB/SEM dual-beam workstation (Helios 660 NanoLab, FEI) using the secondary electron imaging mode. The grain size was measured by the intercept method[31] on the SEM image of fracture surfaces. Energy-dispersive X-ray spectroscopy (EDS) was conducted by an EDS detector (Octane Super, EDAX) to reveal the element distribution. The real density of the $(Hf_{0.2}Zr_{0.2}Ta_{0.2}Nb_{0.2}Ti_{0.2})C$ samples was measured by the Archimedes method on a Mettler Toledo AT201 digital analytical balance. The relative density was determined from the porosity of the sample that was measured from the SEM images. During the thermal stability test, the fine-grained $(Hf_{0.2}Zr_{0.2}Ta_{0.2}Nb_{0.2}Ti_{0.2})C$ samples were heated to the desired temperature in a tube furnace (1700X, MTI). To determine the grain growth kinetics, the samples were annealed in Ar atmosphere at 1300 and 1600°C, respectively.

The Vickers hardness was measured on a hardness tester (Tukon 2500, Wilson) with a 9.8 N load and a 15 sec dwell time. The samples were polished by diamond lapping films of 15, 9, 6, 3 and 1 μm to mirror finish. The bending strength was measured by the three-point bending test using rectangular bars of $18 \times 3 \times 4$ mm^3. The fracture toughness was measured by the single-edge notched beam (SENB) method using rectangular bars ($18 \times 3 \times 4$ mm^3) with a notch of 1 mm depth and a 0.3 mm width in the center. The span size of the samples was 15 mm the crosshead speed of the tests was 0.2 mm/min. The fracture toughness was calculated based on the Equation (33):

$$K = \frac{3P\,(S/W)\,\alpha^{1/2}\left(1.99 - \alpha\,(1-\alpha)\left(2.15 - 3.93\alpha + 2.7\alpha^2\right)\right)}{BW^{1/2}\left(2 + (1+2\alpha)(1-\alpha)^{3/2}\right)}, \quad (1)$$

where $\alpha = a/W$, B is the thickness, W is the width, a is the notch depth, S is the support span, and P is the load.

3 | RESULTS AND DISCUSSIONS

### 3.1 | Phase and microstructure characterizations

The $(Hf_{0.2}Zr_{0.2}Ta_{0.2}Nb_{0.2}Ti0_{0.2})C$ samples prepared under different SPS conditions are listed in Table 1. The sample number C-1 refers to the coarse-grained sample fabricated using the coarse powders. The sample numbers F-1, F-2, and F-3 are the fine-grain samples fabricated using fine powders under different SPS conditions. The density of F-1 is close to that of C-1, but those of F-2 and F-3 are much lower.

XRD of the $(Hf_{0.2}Zr_{0.2}Ta_{0.2}Nb_{0.2}Ti_{0.2})C$ samples fabricated under different SPS conditions are shown in Figure 1A. All coarse- and fine-grained samples show the formation of a single-phase structure. XRD peaks can be well-indexed as a rock-salt structure with space group $Fm\bar{3}m$. The Rietveld refinement of the high-resolution neutron diffraction fits the rock-salt average structure model (Figure 1B), where the C atoms stays at the (0,0,0) crystallographic site and the metal elements are mixed at the (1/2,1/2,1/2) site, with a fully disorder in long-range scale. The lattice parameter is measured as $a = 4.4879(2)$Å via the Rietveld refinement. There are no additional peaks observed from a possible super lattice (a long-range ordering) of the rock-salt average structure. The well-matched intensity fitting excludes the occupation in other interstitial sites. With neutron's unique sensitivity to differentiate neighboring elements, it agrees that all the five transition-metal elements are disorderedly distributed in the same crystallographic site of the rock-salt lattice in the long-range scale, resulting in the high configurational entropy. The complex local lattice distortions, compositional inhomogeneity, and ordering may exist in the short-range scale due to the mix of multiple species elements, however, they do not change the long-range disordering or the average structure in the synthesized carbide. The local structure study is out of the scope of this paper and will be performed

(A)

(B)
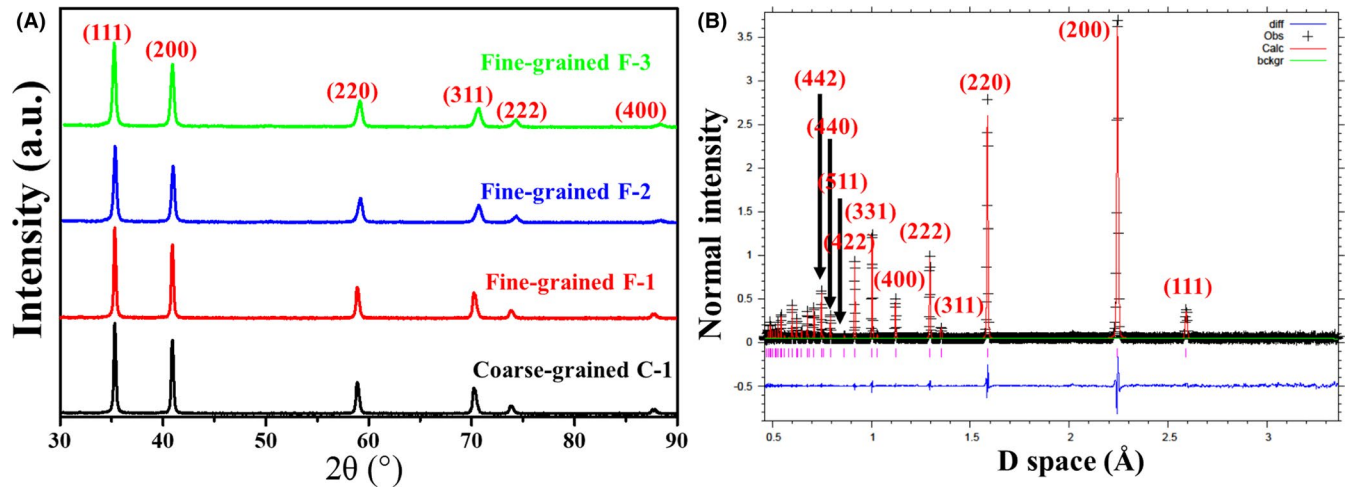
FIGURE 1 Phase characterizations of $(Hf_{0.2}Zr_{0.2}Ta_{0.2}Nb_{0.2}Ti_{0.2})C$ samples: (A) X-ray diffraction of the coarse- (C-1) and fine-grained samples (F-1 to F-3); (B) neutron diffraction and Rietveld refinement of the coarse-grained sample C-1
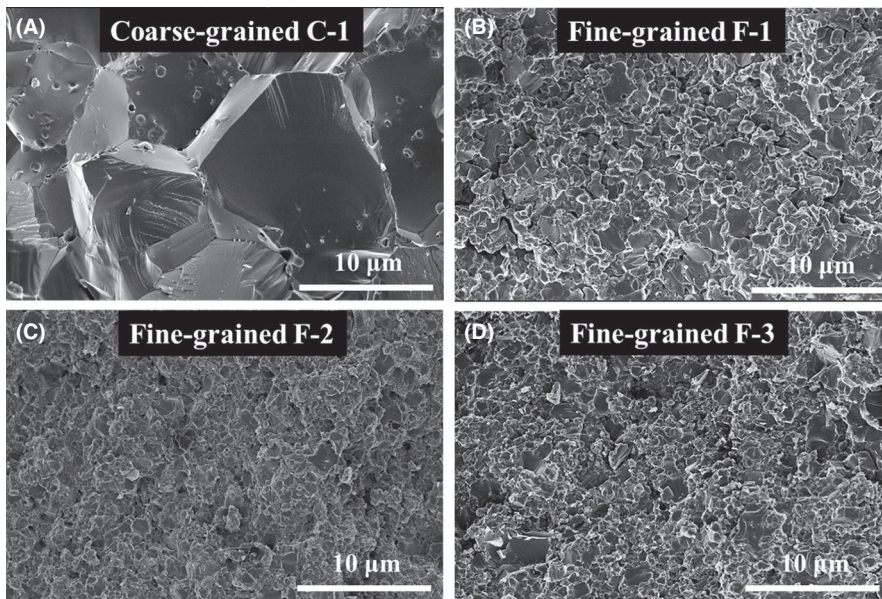
FIGURE 2 SEM images of the fracture surfaces of (A) coarse-grained C-1, (B) fine-grained F-1, (C) fine-grained F-2, and (D) fine-grained F-3 samples

in the future work. The neutron diffraction patterns along the directions in parallel or normal to sample surface was further compared to be the same, which suggests the grains having random orientations without texture in the SPSed $(Hf_{0.2}Zr_{0.2}Ta_{0.2}Nb_{0.2}Ti_{0.2})C$ samples.

SEM images of the fracture surfaces of the $(Hf_{0.2}Zr_{0.2}Ta_{0.2}Nb_{0.2}Ti_{0.2})C$ samples are presented in Figure 2, which revealed equiaxed grains. Because the fracture mode of HEC is intergranular, the fracture surface can be used to reveal the grain size. The grain sizes of fine-grained samples range from 400 to 600 nm (Table 1). In contract, the average grain size of the coarse-grained sample is 16.5 μm. The element distribution in the $(Hf_{0.2}Zr_{0.2}Ta_{0.2}Nb_{0.2}Ti_{0.2})C$ samples is shown in Figure 3A,B. Both the coarse-grained and fine-grained samples show homogenous distributions of Ta, Zr, Ti,

Nb, Hf, and C elements at the micrometer level. Figure 3C,D shows the EDS spectrum of coarse-grained C-1 and fine-grained F-1 HEC samples. Based on the EDS results, the oxygen concentration is 2.2 ~ 3.2 atomic percent. The ratio of Ti, Ta, Nb, Zr, and Hf is close to the stoichiometric ratio. No Fe or Cr contamination from the ball milling process was found. TEM EDS mapping of element distribution inside one grain and in a triple junction is shown in Figure 4. The combination of EDS analysis in SEM and TEM covered the scale of element distribution from micrometer to nanometer, in which no element segregation was observed. Figure 4C shows the high-resolution TEM (HRTEM) image of the fine-grained F-1 HEC. The lattice spacing of the (-1 1 -1) plane was measured to be 0.26 nm. The lattice constant can be calculated to be 0.45 nm, which is close to that measured from neutron

FIGURE 3 Energy-dispersive X-ray spectroscopy (EDS) mapping of Ta, Zr, Ti, Nb, Hf, and C element distribution in (A) coarse-grained C-1 and (B) fine-grained F-1 $(Hf_{0.2}Zr_{0.2}Ta_{0.2}Nb_{0.2}Ti_{0.2})C$ samples. EDS spectrum of the polished surfaces of (C) coarse-grained C-1 and (D) fine-grained F-1 HEC samples

(A) **Coarse-grained C-1 HEC**
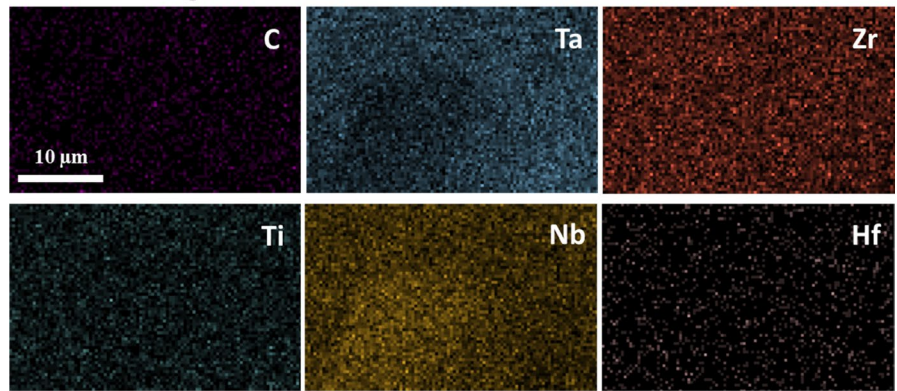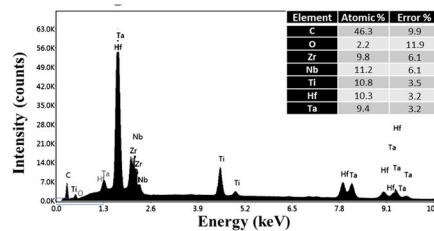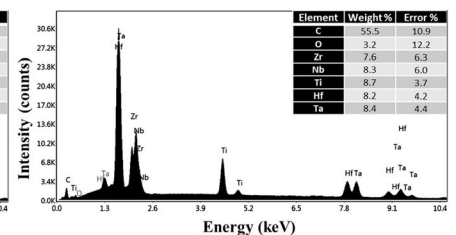
(B) **Fine-grained F-1 HEC**
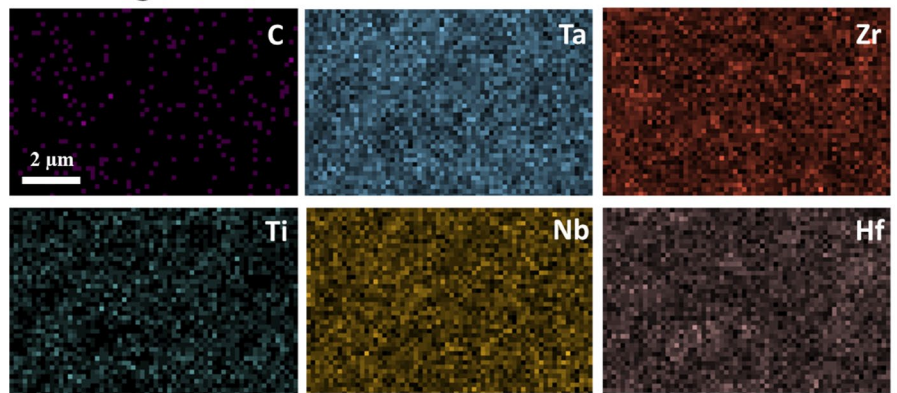
(C) **Coarse-grained HEC**

(D) **Fine-grained F-1 HEC**

diffraction. The combination of XRD, neutron diffraction, and EDS results confirmed the formation of the high-entropy phase $(Hf_{0.2}Zr_{0.2}Ta_{0.2}Nb_{0.2}Ti_{0.2})C$ in both the coarse- and fine-grained samples. No secondary phase or element segregation was observed in these samples.

3.2 | Thermal stability of the fine-grained $(Hf_{0.2}Zr_{0.2}Ta_{0.2}Nb_{0.2}Ti_{0.2})C$

Figure 5A-E are the typical images of the fracture surfaces, which shows the grain morphology in the fine-grained F-1 (Hf $_{0.2}Zr_{0.2}Ta_{0.2}Nb_{0.2}Ti_{0.2})C$ sample before and after annealing at 1300 and 1600°C for 5 and 10 hours. The average grain size increased slightly from 0.57 μm before annealing, to 0.77 μm after annealing at 1300°C for 10 hours, and to 0.86 μm after annealing at 1600°C for 10 hours (Figure 5F). Thus, the grain growth at 1300 and 1600°C was small, suggesting that the

fine-grained $(Hf_{0.2}Zr_{0.2}Ta_{0.2}Nb_{0.2}Ti_{0.2})C$ sample has superior thermal stability at high temperatures.

Grain growth of TiC during heating has been reported by Kislyi et al[31] which showed that annealing at 1400-1600°C leads to the formation of large TiC grains and precipitation of excess carbon on grain boundaries. $(Hf_{0.2}Zr_{0.2}Ta_{0.2}Nb_{0.2}Ti_{0.2})$ C does not have these microstructure changes, suggesting that it has a higher thermal stability than TiC. The higher thermal stability of high entropy oxides has been also reported by Zhao et al,[32] which showed that the grain growth rate of high entropy ceramic $(La_{0.2}Ce_{0.2}Nd_{0.2}Sm_{0.2}Eu_{0.2})_2Zr_2O_7$ was much lower than that of $La_2Zr_2O_7$. After heating at 1500°C for 18 hours, the average grain size of $(La_{0.2}Ce_{0.2}Nd_{0.2}Sm_{0.2}Eu_{0.2})_2Zr_2O_7$ only increased from 1.69 to 3.92 μm, while the average grain size of $La_2Zr_2O_7$ increased significantly from 1.96 to 8.89 μm.

The experimental results presented here suggest that the grain growth in nanocrystalline ceramics may be retarded
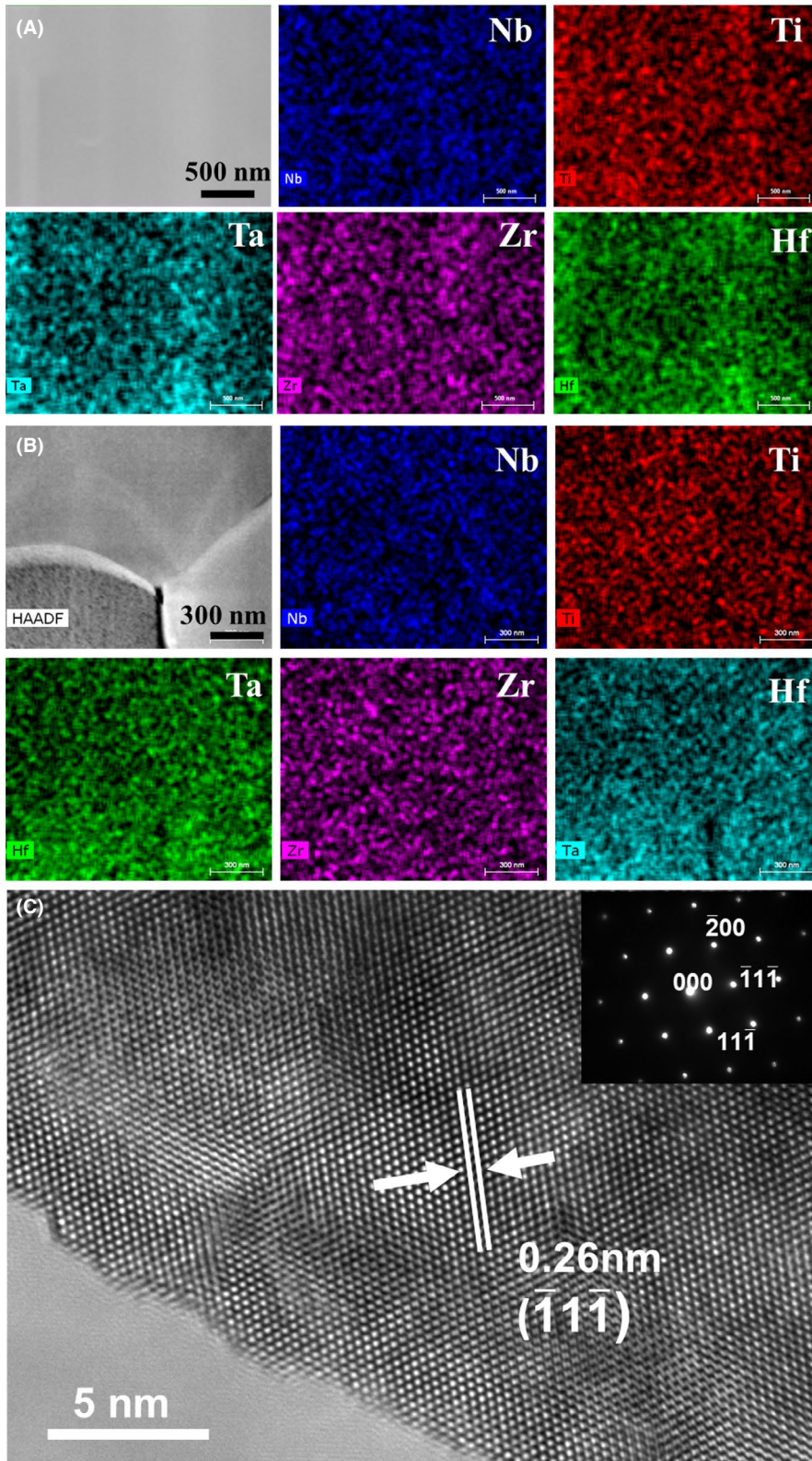
FIGURE 4 TEM energy-dispersive X-ray spectroscopy mapping of element distribution (A) inside one grain and (B) in the triple junction of the fine-grained F-1 HEC sample, and (C) HRTEM image of the fine-grained F-1 $(Hf_{0.2}Zr_{0.2}Ta_{0.2}Nb_{0.2}Ti_{0.2})$ C. Insert: selected area electron diffraction pattern

by the high-entropy effects. This may be theoretically explained by the fact that the high-entropy effects can reduce both the driving force (grain-boundary energy) and kinetics (grain-boundary migration rate) of grain growth. The compositional complexity in HECs can reduce the grain boundary energy by increasing grain boundary complexity according to the equation of grain boundary energy (γ_{GB})[33]:

$$\gamma_{GB} = e^{xs} - S^{xs}T - \sum_i \mu_i \Gamma_i, \qquad (2)$$
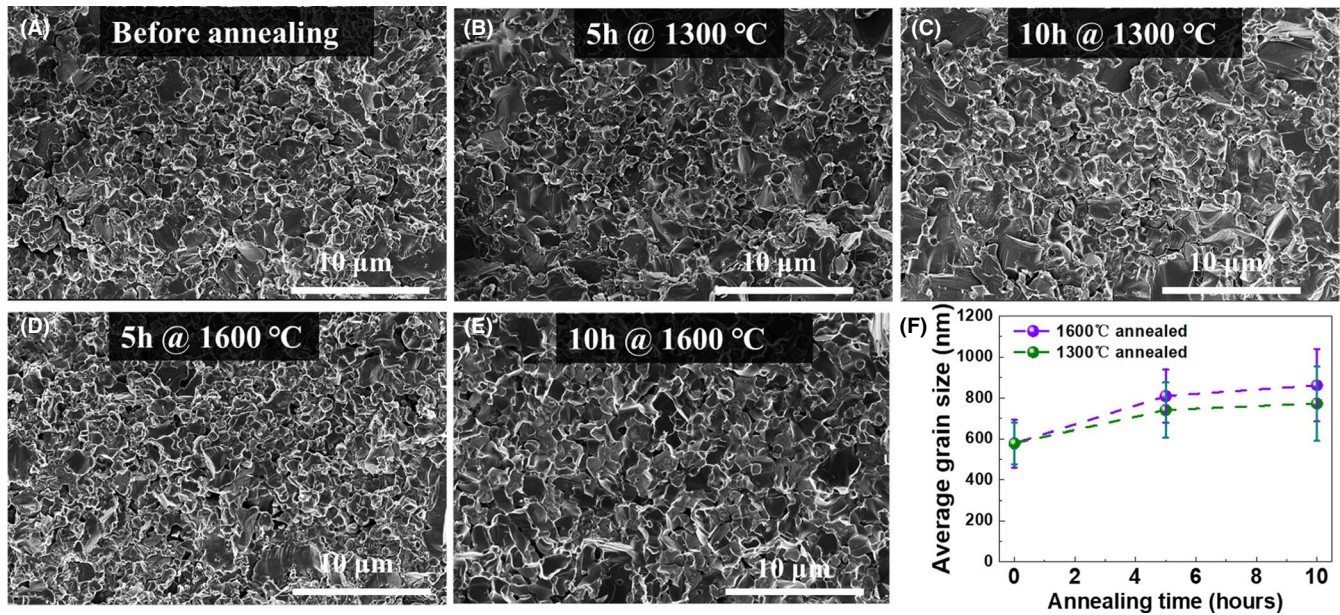
FIGURE 5 SEM images of the grain morphology in fine-grained F-1 $(Hf_{0.2}Zr_{0.2}Ta_{0.2}Nb_{0.2}Ti_{0.2})C$ sample: (A) before annealing, (B) after annealing at 1300°C for 5 h, (C) after annealing at 1300°C for 10 h, (D) after annealing at 1600°C for 5 h, and (E) after annealing at 1600°C for 10 h. (F) the average grain size as a function of annealing time at 1300 and 1600°C, respectively

FIGURE 6 SEM image of the Vickers indentation of (A) fine-grained F-1 and (B) coarse-grained C-1 $(Hf_{0.2}Zr_{0.2}Ta_{0.2}Nb_{0.2}Ti_{0.2})C$ samples
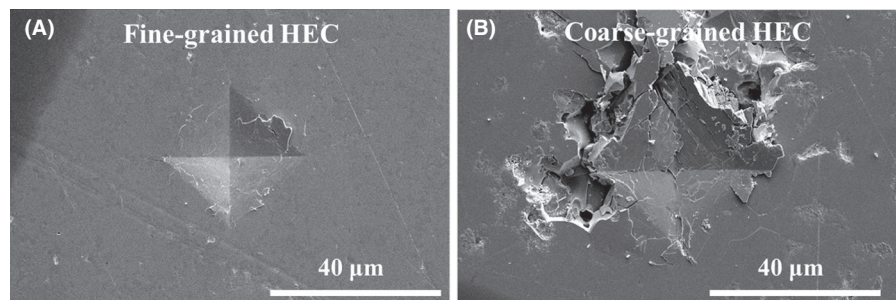

where e^{xs} the is internal energy, S^{xs} the is entropy, T is the temperature, μ_i is the chemical potential of the i-th element, and Γ_i is the adsorption of the i-th component.[34,35] In addition, the grain-boundary migration rate is also hindered by the sluggish diffusion at grain boundaries. In high-entropy materials, each cation site in the sublattice is surrounded by different metal atoms, which leads to different bonds and lattice potential energies. The fluctuation of lattice potential energy can produce atomic traps to slow down the diffusion of atoms, resulting in sluggish diffusion in high-entropy ceramics.[36] The high-entropy effect on retarding grain growth has been also observed by modeling and experiments in metallic HEAs.[35] Beke et al suggest that the activation energy of diffusion in CoCrFeMnNi HEAs is higher than Ni or Fe due to the fluctuation of lattice potential energy that produces atomic traps leading to the sluggish diffusion.[37] Zhou et al showed that Ni-containing HEAs (eg, $Ni_{29}Fe_{23}Co_{23}Cr_{23}Zr_2$ and $Ni_{25}Fe_{23}Co_{23}Cr_{23}Mo_2Nb_2Zr_2$) can maintain nanometer grain size at temperatures up to 800°C, while rapid grain growth is observed in pure Ni at a temperature as low as 300°C.[34]

3.3 | Mechanical properties of fine-grained $(Hf_{0.2}Zr_{0.2}Ta_{0.2}Nb_{0.2}Ti_{0.2})C$

The Vickers hardness of the $(Hf_{0.2}Zr_{0.2}Ta_{0.2}Nb_{0.2}Ti0_{0.2})C$ samples prepared under different SPS conditions is presented in Table 1. The hardness of the fined-grained sample F-1 is slightly higher (about 5%) than the coarse-grained sample C-1. However, the hardness of F-2 and F-3 are much lower than F-1, which are presumably related to their lower density and higher porosity.

Figure 6 shows the SEM images of the Vickers indentations on fine-grained (F-1) and coarse-grained (C-1) $(Hf_{0.2}Zr_{0.2}Ta_{0.2}Nb_{0.2}Ti_{0.2})C$ samples. The Vickers indentation method was used to compare the coarse-grained and fine-grained HEC under same indentation load. This technique has been reported by Wang et al[38] to compare the surface crack length of nano-grained and coarse-grained YAG ceramics generated by Vickers indentations. Severe cracking and grain pull-out occurred in the coarse-grained sample around the Vickers indentation (Figure 6B). In contrast, no
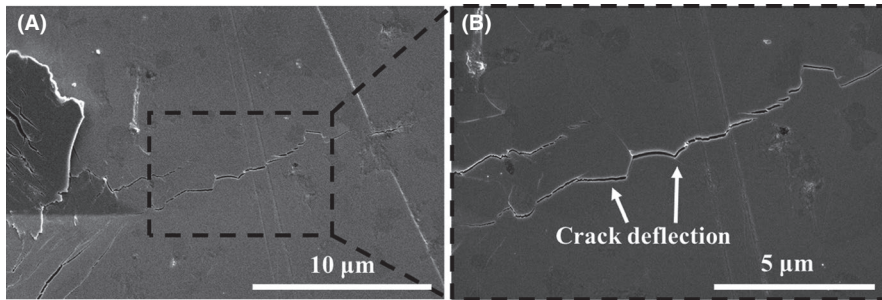
FIGURE 7 Crack deflection as the toughening mechanism in fine-grained F-1 $(Hf_{0.2}Zr_{0.2}Ta_{0.2}Nb_{0.2}Ti_{0.2})C$ sample
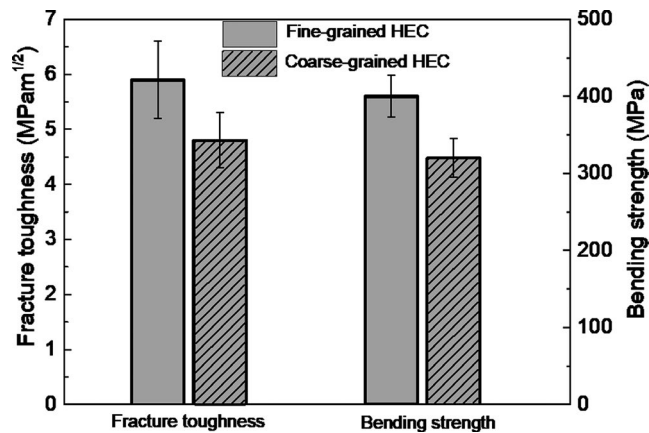

FIGURE 8 Comparison of fracture toughness and bending strength of the fine-grained F-1 and coarse-grained C-1 $(Hf_{0.2}Zr_{0.2}Ta_{0.2}Nb_{0.2}Ti_{0.2})C$ samples

significant cracking was observed in the fine-grained sample around the indentations (Figure 6A), indicating its higher cracking resistance and fracture toughness than the coarse-grained sample. The main difference between the coarse- and fine-grained samples is the higher grain-boundary volume in the fine-grained sample. The increase in the grain-boundary volume can result in more intergranular fracture instead of cleavage in ceramic materials.[39,40] The enlarged view of microcracks in the edge of the Vickers indentation in the fine-grained sample revealed crack deflection by grain boundaries (Figure 7), which is a mechanism that allow more elastic energy to be released and thus improve the cracking resistance.

Because F-2 and F-3 have lower density and hardness than F-1, only F-1 was selected to represent the fine-grained sample to prepare the specimens for three-point bending and SENB tests. Figure 8 compares the measured fracture toughness and bending strength of the fine- (F-1) and coarse-grained (C-1) $(Hf_{0.2}Zr_{0.2}Ta_{0.2}Nb_{0.2}Ti_{0.2})C$ samples. The average bending strength of the fine-grained sample is 400 MPa, which is 25% higher than that of the coarse-grained one.

The average fracture toughness of the fine-grained (F-1) $(Hf_{0.2}Zr_{0.2}Ta_{0.2}Nb_{0.2}Ti_{0.2})C$ sample is measured to be 5.9 MPam$^{1/2}$, which is 20% higher than that of the coarse-grained sample. The scattering of fracture toughness values is shown in Figure 8. This result is consistent with the high cracking resistance in the fine-grained sample (Figure 6). Figure 9 shows the comparison of the top view and side views of the fracture surfaces of the coarse- and fine-grained $(Hf_{0.2}Zr_{0.2}Ta_{0.2}Nb_{0.2}Ti_{0.2})C$ samples. The main fracture
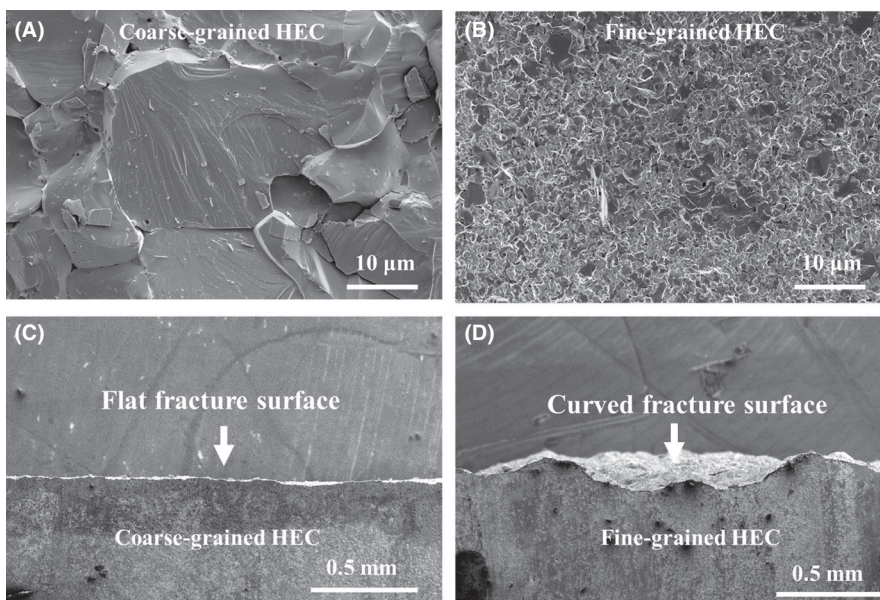
FIGURE 9 Plan view of the fracture surface of (A) coarse-grained C-1 and (B) fine-grained F-1 samples. Side view of the fracture surface of (C) coarse-grained C-1 and (D) fine-grained F-1 samples

mode in the coarse-grained sample is transgranular cleavage (Figure 8A), while that in the fine-grained sample is intergranular cracking (Figure 8B). This is further confirmed by the straight crack path in the coarse-grained sample (Figure 8C) compared to the curved fracture path in the fine-grained sample (Figure 8D).

The Griffith equation of the relationship between strength, fracture toughness, and flaw size in ceramics is[41]:

$$\sigma_f = K_{IC} \Big/ \left(Y \sqrt{\pi a} \right), \tag{3}$$

where σ_f is the strength, K_{IC} is the fracture toughness, Y is a geometric factor ($Y = 1$-1.1), and a is half of the flaw size. Based on the measured strength and fracture toughness results, the flaw sizes of the fine- and coarse-grained $(Hf_{0.2}Zr_{0.2}Ta_{0.2}Nb_{0.2}Ti_{0.2})$ C samples are calculated to be 138 and 150 μm respectively. The calculated flaw sizes are much larger than the grain sizes in both samples. This indicates that the flaws to initiate the cracks in these HEC samples most likely come from the pre-existing large pores or cracks in a dimension of 100-200 μm, which may be formed during the fabrication or machining processes.

4 | CONCLUSIONS

1. HECs with submicron grain sizes of 400 to 600 nm were fabricated by SPS using the two-step sintering process. Coarse-grain HEC with a grain size of 16.5 μm were also fabricated for comparison.
2. The SPS fabricated sample with a single phase of rock salt structure, disordered transition-metal element arrangement, and random grain orientations was confirmed by X-ray and neutron diffractions. No secondary phase or element segregation was observed.
3. The concept proposed to inhibit the grain growth in ceramic materials by the high-entropy effects was demonstrated. The grain growth kinetics in the fine-grained HECs is small at 1300 and 1600°C, which is possibly related to the compositional complexity and sluggish diffusion in HEC.
4. The fined-grained HECs showed higher cracking resistance to Vickers indentation than the coarse-grained one due to the micromechanistic mechanisms such as crack deflection.
5. The bending strength and fracture toughness of fine-grained HECs are 25% and 20% higher, respectively, than the coarse-grained HEC. The main fracture mode transited from the transgranular cleavage in the coarse-grained HEC to intergranular cracking in the fine-grained HEC.
6. These findings provide important guidance on the development of high-performance ceramic materials with submicron grain sizes using the novel high-entropy strategy.

ORCID

Fei Wang [ID] https://orcid.org/0000-0002-8283-0651
Bai Cui [ID] https://orcid.org/0000-0002-0585-6698

REFERENCES

1. Gild J, Zhang Y, Harrington T, Jiang S, Hu T, Quinn MC, et al. High-entropy metal diborides: a new class of high-entropy materials and a new type of ultrahigh temperature ceramics. Sci Rep. 2016;6:37946.
2. Ye B, Wen T, Nguyen MC, Hao L, Wang C-Z, Chu Y. First-principles study, fabrication and characterization of $(Zr_{0.25}Nb_{0.25}Ti_{0.25}V_{0.25})$ C high-entropy ceramics. Acta Mater. 2019;170:15–23.
3. Castle E, Csanádi T, Grasso S, Dusza J, Reece M. Processing and properties of high-entropy ultra-high temperature carbides. Sci Rep. 2018;8(1):1–12.
4. Feng L, Fahrenholtz WG, Hilmas GE, Zhou Y. Synthesis of single-phase high-entropy carbide powders. Scr Mater. 2019;162:90–3.
5. Zhou J, Zhang J, Zhang F, Niu B, Lei L, Wang W. High-entropy carbide: a novel class of multicomponent ceramics. Ceram Int. 2018;44(17):22014–8.
6. Yan X, Constantin L, Lu Y, Silvain J-F, Nastasi M, Cui B. $(Hf_{0.2}Zr_{0.2}Ta_{0.2}Nb_{0.2}Ti_{0.2})$ C high-entropy ceramics with low thermal conductivity. J Am Ceram Soc. 2018;101(10):4486–91.
7. Sarker P, Harrington T, Toher C, Oses C, Samiee M, Maria J-P, et al. High-entropy high-hardness metal carbides discovered by entropy descriptors. Nat Commun. 2018;9(1):1–10.
8. Demirskyi D, Borodianska H, Suzuki TS, Sakka Y, Yoshimi K, Vasylkiv O. High-temperature flexural strength performance of ternary high-entropy carbide consolidated via spark plasma sintering of TaC, ZrC and NbC. Scr Mater. 2019;164:12–6.
9. Yang Y, Wang W, Gan G-Y, Shi X-F, Tang B-Y. Structural, mechanical and electronic properties of (TaNbHfTiZr) C high entropy carbide under pressure: Ab initio investigation. Phys B Condens Matter. 2018;550:163–70.
10. Ye B, Wen T, Liu D, Chu Y. Oxidation behavior of $(Hf_{0.2}Zr_{0.2}Ta_{0.2}Nb_{0.2}Ti_{0.2})$ C high-entropy ceramics at 1073–1473 K in air. Corros Sci. 2019;153:327–32.

11. Ye B, Wen T, Chu Y. High-temperature oxidation behavior of $(Hf_{0.2}Zr_{0.2}Ta_{0.2}Nb_{0.2}Ti_{0.2})$ C high-entropy ceramics in air. J Am Ceram Soc. 2020;103(1):500–7.

12. Tan Y, Chen C, Li S, Han X, Xue J, Liu T, et al. Oxidation behaviours of high-entropy transition metal carbides in 1200° C water vapor. J Alloys Compd. 2020;816:152523.

13. Mayrhofer PH, Kirnbauer A, Ertelthaler P, Koller CM. High-entropy ceramic thin films; a case study on transition metal diborides. Scr Mater. 2018;149:93–7.

14. Trunec M, Chlup Z. Higher fracture toughness of tetragonal zirconia ceramics through nanocrystalline structure. Scr Mater. 2009;61(1):56–9.

15. Bravo-Leon A, Morikawa Y, Kawahara M, Mayo MJ. Fracture toughness of nanocrystalline tetragonal zirconia with low yttria content. Acta Mater. 2002;50(18):4555–62.

16. Gleiter H. Nanocrystalline materials. In: Bunk W. G. J, editor. Advanced Structural and Functional Materials. Berlin, Heidelberg: Springer; 1991. p. 1–37.

17. Jeong DH, Erb U, Aust KT, Palumbo G. The relationship between hardness and abrasive wear resistance of electrodeposited nanocrystalline Ni–P coatings. Scr Mater. 2003;48(8):1067–72.

18. Xu X, Nishimura T, Hirosaki N, Xie R-J, Yamamoto Y, Tanaka H. Superplastic deformation of nano-sized silicon nitride ceramics. Acta Mater. 2006;54(1):255–62.

19. Mayo MJ. Synthesis and applications of nanocrystalline ceramics. Mater Des. 1993;14(6):323–9.

20. Louat NP. On the theory of normal grain growth. Acta Metall. 1974;22(6):721–4.

21. Gertsman VY, Birringer R. On the room-temperature grain growth in nanocrystalline copper. Scr Metall Mater. 1994;30(5):577–81.

22. Raabe D, Hantcherli L. 2D cellular automaton simulation of the recrystallization texture of an IF sheet steel under consideration of Zener pinning. Comput Mater Sci. 2005;34(4):299–313.

23. Liu F, Kirchheim R. Nano-scale grain growth inhibited by reducing grain boundary energy through solute segregation. J Cryst Growth. 2004;264(1–3):385–91.

24. Wang X-H, Chen P-L, Chen I-W. Two-step sintering of ceramics with constant grain-size, I. Y_2O_3. J Am Ceram Soc. 2006;89(2):431–7.

25. Chen I-W, Wang X-H. Sintering dense nanocrystalline ceramics without final-stage grain growth. Nature. 2000;404(6774):168–71.

26. Lee Y-I, Kim Y-W, Mitomo M, Kim D-Y. Fabrication of dense nanostructured silicon carbide ceramics through two-step sintering. J Am Ceram Soc. 2003;86(10):1803–5.

27. Wang C-J, Huang C-Y, Wu Y-C. Two-step sintering of fine alumina–zirconia ceramics. Ceram Int. 2009;35(4):1467–72.

28. An K, Skorpenske HD, Stoica AD, Ma D, Wang X-L, Cakmak E. First in situ lattice strains measurements under load at VULCAN. Metall Mater Trans A. 2011;42(1):95–9.

29. Larson AC, Von Dreele RB. General structure analysis system (GSAS) (Report LAUR 86–748). Los Alamos Natl Lab N M USA; 2004.

30. Toby BH. EXPGUI, a graphical user interface for GSAS. J Appl Crystallogr. 2001;34(2):210–3.

31. Kislyi PS, Golubyak LS, Zaverukha OV. Effect of annealing on the structure and properties of fused titanium carbide. Sov Powder Metall Met Ceram. 1970;9(10):845–8.

32. Zhao Z, Xiang H, Dai F-Z, Peng Z, Zhou Y. $(La_{0.2}Ce_{0.2}Nd_{0.2}Sm_{0.2}Eu_{0.2})_2Zr_2O_7$: A novel high-entropy ceramic with low thermal conductivity and sluggish grain growth rate. J Mater Sci Technol. 2019;35(11):2647–51.

33. Abrams H. Grain size measurement by the intercept method. Metallography. 1971;4(1):59–78.

34. Zhou N, Hu T, Huang J, Luo J. Stabilization of nanocrystalline alloys at high temperatures via utilizing high-entropy grain boundary complexions. Scr Mater. 2016;124:160–3.

35. Zhou N, Hu T, Luo J. Grain boundary complexions in multicomponent alloys: challenges and opportunities. Curr Opin Solid State Mater Sci. 2016;20(5):268–77.

36. Tsai K-Y, Tsai M-H, Yeh J-W. Sluggish diffusion in Co–Cr–Fe–Mn–Ni high-entropy alloys. Acta Mater. 2013;61(13):4887–97.

37. Beke DL, Erdélyi G. On the diffusion in high-entropy alloys. Mater Lett. 2016;164:111–3.

38. Wang HM, Huang ZY, Jiang JS, Liu K, Duan MY, Lu ZW, et al. Unique mechanical properties of nano-grained YAG transparent ceramics compared with coarse-grained partners. Mater Des. 2016;105:9–15.

39. Xiao C, Mirshams RA, Whang SH, Yin WM. Tensile behavior and fracture in nickel and carbon doped nanocrystalline nickel. Mater Sci Eng A. 2001;301(1):35–43.

40. Wang F, Zhang Y, Lu J, Zang P, Wang J, Zhang X. In situ observation of intergranular fracture propagation in nanocrystalline freestanding ultrathin tungsten film. Mater Lett. 2014;122:334–7.

41. Doremus RH, Pavelchek EK. Griffith fracture equation—an experimental test. J. Appl. Phys. 1975;46:4096–7.